Highly anisotropic geometrical Hall effect via f-d exchange fields in doped pyrochlore molybdates

Hikaru Fukuda,[1] Kentaro Ueda [ORCID],[1,*] Yoshio Kaneko,[2] Ryosuke Kurihara,[2,3] Atsushi Miyake,[4] Kosuke Karube,[2] Masashi Tokunaga [ORCID],[2,4] Yasujiro Taguchi [ORCID],[2] and Yoshinori Tokura [ORCID][1,2,5]

[1]*Department of Applied Physics, University of Tokyo, Bunkyo, Tokyo 113-8656, Japan*
[2]*RIKEN Center for Emergent Matter Science, Wako, Saitama 351-0198, Japan*
[3]*Department of Physics, Tokyo University of Science, Noda, Chiba 278-0022, Japan*
[4]*Institute for Solid State Physics (ISSP), University of Tokyo, Kashiwa, Chiba 277-8581, Japan*
[5]*Tokyo College, The University of Tokyo, Tokyo 113-8656, Japan*

When a conduction electron couples with a non-coplanar localized magnetic moment, the real-space Berry curvature is exerted to cause the geometrical Hall effect, which is not simply proportional to the magnetization. So far, it has been identified in the case mostly where the non-coplanar magnetic order is present on the sublattice of conduction electrons. Here, we demonstrate that the geometrical Hall effect shows up even without long-range magnetic order of conduction electrons, as induced by non-coplanar exchange fields from the localized magnetic moments, in hole-doped pyrochlore molybdates $(Tb_{1-x}Ca_x)_2Mo_2O_7$. We find that the geometrical Hall effect is markedly anisotropic with respect to the applied magnetic field direction, which is in good accordance with the field-dependent magnitude and sign change of the real-space scalar spin chirality of local Tb moments. These results may facilitate the understanding of emergent electromagnetic responses induced by the Kondo-like coupling between conduction electrons and local spins in a broad material class.

I. INTRODUCTION

Noncollinear or non-coplanar complex magnetic structures in solids are proven to play a fundamentally important role in their spin-related quantum transport and multiferroic properties [1,2]. A representative example is the scalar spin chirality (SSC), which is defined by $\chi_{ijk} = S_i \cdot (S_j \times S_k)$ for three neighboring-site spins: S_i, S_j, and S_k. As a conduction electron moves over a non-coplanar spin texture with finite SSC, it is endowed with the nontrivial quantum phase (Berry phase) and hence experiences the emergent magnetic field, which can be far beyond a real magnetic field [3–5]. One of the most common outcomes of the SSC is the unconventional Hall effect, termed the geometrical Hall effect (GHE) [5]. In the case where the mean free path is sufficiently longer than the magnetic period, both the anomalous Hall effect and the GHE are appropriately captured by the momentum space picture where the anticrossing points (e.g., Weyl nodes) are associated with the Berry curvature due to the spin-orbit coupling (Karplus-Luttinger intrinsic mechanism) and the SSC [6,7]. In contrast, as the magnetic period is longer than the mean free path, electrons hop around the spin triad in the real space and feel the emergent field $B_{\mathrm{eff}} = h n_{ijk} \chi_{ijk}/eS$, where n_{ijk} is the normal vector to the spin triad plane and S is the area of the spin triad, as exemplified by the magnetic skyrmion lattice [8,9].

Among a variety of non-coplanar magnets, pyrochlore molybdates $R_2Mo_2O_7$ (R being a trivalent rare-earth or Y ion) offer an ideal platform to study the correlation between charge transport and non-coplanar magnetism, because of a variety of magnetic/electronic phases [10–12]. The pyrochlore lattice consists of corner-linked tetrahedra with R ions and Mo ions, each of which is displaced by half a unit cell [Fig. 1(a)]. The most well investigated is $Nd_2Mo_2O_7$ with the largest-size R ion possible and hence with relatively small electron correlation. It is metallic in the whole temperature range and undergoes the ferromagnetic transition at 90 K, presumably due to the double-exchange-like mechanism of Mo $4d$ electrons [13]. Additionally, the Nd $4f$ magnetic moments, which host Ising anisotropy along the local $\langle 111 \rangle$ direction, begin to freeze below around 40 K. Therefore, the Mo spins are slightly tilted ($\sim 5°$–$10°$) via the f-d magnetic interaction at low temperatures, resulting in the Mo spins with finite SSC [Fig. 1(b)] [4]. Because of such anisotropy for R $4f$ moments, various configurations are realized under the external magnetic field [14,15]. For instance, as the field is applied along the [100] direction, two of four magnetic moments point out of the tetrahedron, while the other two point inwards, termed the 2-in 2-out configuration. On the other hand, the field along [111] favors the 3-in 1-out state, as displayed in the bottom panel in Fig. 1(b). The anisotropy of Hall response in $Nd_2Mo_2O_7$ is understood in terms of the 2-in 2-out or 3-in 1-out like habit of the Mo $4d$ spins transmitted from the corresponding change of the Nd $4f$ configuration [16]. Such a case where the Mo $4d$ ferromagnetic orders are slightly modulated by the R $4f$ moments is termed the strong coupling, which has been

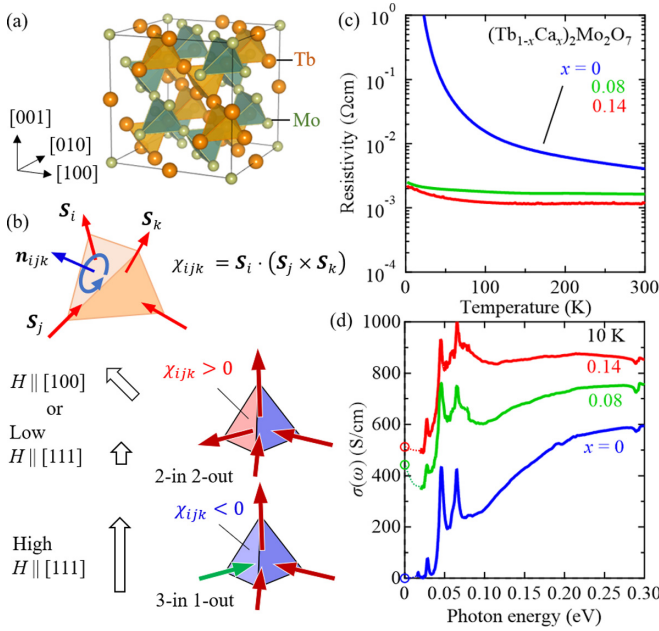FIG. 1. (a) Crystal structure of pyrochlore-type $Tb_2Mo_2O_7$. (b) Definition of the SSC $\chi_{ijk} = S_i \cdot (S_j \times S_k)$ in a tetrahedron with Tb spins S_i, S_j, and S_k on its vertices. The middle (bottom) figure shows χ_{ijk} in each triangle plane of a tetrahedron for the 2-in 2-out (3-in 1-out) state. The color of the plane corresponds to the sign of χ_{ijk} when we take $n_{ijk} \cdot H > 0$. In these figures, the $H \parallel$ [111] case is assumed. (c) Temperature dependence of resistivity for $(Tb_{1-x}Ca_x)_2Mo_2O_7$. (d) Optical conductivity spectra below 0.3 eV at 10 K for $(Tb_{1-x}Ca_x)_2Mo_2O_7$.

FIG. 2. (a) Measurement setup for magnetic transport properties. Magnetic field dependence of (b) resistivity for both $H \parallel$ [100] and $H \parallel$ [111], (c) Hall resistivity for $H \parallel$ [100], (d) Hall resistivity for $H \parallel$ [111], (e) anisotropic ratio of Hall resistivity between $H \parallel$ [100] and $H \parallel$ [111], and (f) magnetization for both $H \parallel$ [100] and $H \parallel$ [111] at several temperatures.

extensively studied so far [4,17]. On the other hand, little is known for the weak-coupling regime, where the Mo conduction electrons exhibit no spontaneous long-range orders but are weakly influenced by the exchange fields from the R $4f$ moment configuration [18].

Previously, GHE in the weak-coupling regime was studied for the $(Tb_{1-x}Cd_x)_2Mo_2O_7$ polycrystals [19]. It was demonstrated that the Hall response systematically changes as a function of the "density" of SSC in the real space tuned by the doping level of magnetic Tb moments, in accord with the theoretical prediction [18]. However, the exchange-field-induced GHE should be dominated by the R $4f$ moment configuration; for instance, the SSC is expected to change its sign and magnitude between the 2-in 2-out and the 3-in 1-out configuration and, further, to diminish as the R $4f$ moments are forced to align in a collinear manner. Thus, to obtain a deeper insight into the GHE, a field-directional study on the single crystals is required.

In this study, we investigate the magnetotransport properties of $(Tb_{1-x}Ca_x)_2Mo_2O_7$ single crystals to see the role of the real-space SSC in the Hall effect. We successfully synthesize high-quality samples by using the state-of-the-art floating zone furnace equipped with high-power lasers and measure the transport and magnetization at high magnetic fields up to 31 T, which allows us to access a wide range of Tb magnetic states from non-coplanar spin textures to the fully spin-aligned state. We observe the large anisotropy of GHE between the [100] and [111] field directions in the intermediate-
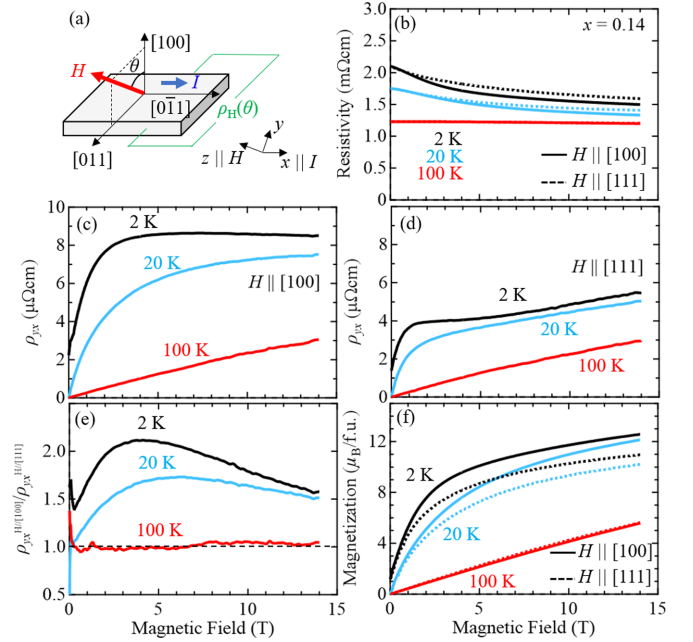
field range, which gradually diminishes at high fields. It can be reasonably explained in terms of the magnitude and sign change of the SSC of localized Tb moments that impose the *f-d* exchange field on the conductive Mo sublattice.

II. EXPERIMENTAL DETAILS

Single crystals were synthesized at ~1880 °C under an argon atmosphere of 0.99 MPa in the laser floating zone furnace [20]. All of them were well characterized by x-ray powder diffraction and energy dispersive x-ray spectroscopy to check the lattice structure and composition. The transport measurement setup is shown in Fig. 2(a). The electric current flows along the [1$\bar{1}$0] crystalline direction. The magnetic field was rotated around the current direction, so that the transport measurements for different orientations could be performed on the same sample. $\theta = 0°$, which is perpendicular to the sample plane, is along the [100] crystalline direction, while $\theta = \pm54.7°$ is along the [111] direction and its equivalent direction. We obtained the Hall resistivity ρ_{yx} by normalizing the measured Hall signal ρ_H for $\theta = \pm54.7°$ divided by $\cos\theta$. We confirm that the deduced ρ_{yx} shows almost the same behavior as another sample with the [111] plane measured under the normal [111] field (see the Appendix, Fig. 5). The transport properties and magnetization up to 14 T were measured by using dc magnets in the Physical Property Measurement System, Quantum Design. Higher-field measurements of magnetotransport and magnetization were performed by using nondestructive pulse magnets energized by capacitor banks and a flywheel dc generator installed at

International MegaGauss Science Laboratory of Institute for Solid State Physics, University of Tokyo.

III. RESULTS AND DISCUSSION

Figure 1(c) shows the temperature dependence of resistivity for three compositions ($x = 0$, 0.08, and 0.14). The resistivity of $x = 0$ rapidly increases as the temperature decreases. Above $x = 0.08$, the resistivity significantly decreases down to the order of 10^{-3} Ω cm. The weak temperature dependence for higher doping reminds us of the high-pressure effect on $Nd_2Mo_2O_7$, which yields the anomalously diffusive metallic state as a result of the strong competition between an antiferromagnetic (spin glass) insulator and ferromagnetic metal states [11]. The optical conductivity spectra at 10 K for several x are displayed in Fig. 1(d). The optical conductivity for $x = 0$ gradually decreases below 0.2 eV, forming a clear charge gap of ~0.05 eV. The observed magnitude of the charge gap is slightly different from the previous one [21], possibly due to the oxygen nonstoichiometry depending on the crystal-growth condition. With increasing x, the optical conductivity gradually increases below $\omega_C \sim 1.5$ eV (see Fig. 5 in the Appendix) accompanied by the closing of the charge gap, in good accordance with the dc conductivity. The absence of the clear Drude peak confirms the diffusive metal state at $x = 0.08$ and 0.14. It is to be noted that the sharp peaks below 0.1 eV are infrared-active phonon modes allowed for cubic pyrochlore lattice [22–24], indicative of a good crystal quality even for the doped metallic samples.

In the following, we focus on the magnetotransport properties of the barely metallic $x = 0.14$ crystal. Figure 2(b) shows the magnetic field dependence of resistivity at several temperatures for $H \parallel$ [111] and [100]. The resistivity is almost independent of the magnetic field at 100 K. Below 20 K, the resistivity gradually decreases with increasing field, likely due to the suppression of spin glass or antiferromagnetic spin fluctuation. Figures 2(c) and 2(d) show the Hall resistivity ρ_{yx} for $H \parallel$ [100] and $H \parallel$ [111], respectively. ρ_{yx} at 100 K is nearly proportional to the magnetic field with little difference between ρ_{yx} for $H \parallel$ [100] and $H \parallel$ [111]. However, the anisotropy becomes evident at low temperatures. At 2 K, as the field increases, ρ_{yx} for $H \parallel$ [100] abruptly increases, reaches a maximum value of ~9 $\mu\Omega$ cm at around 8 T, and then slightly decreases. On the other hand, ρ_{yx} for $H \parallel$ [111] shows a hump at around 2 T and gradually increases as the field is further increased. As can be seen in Fig. 2(e), the anisotropy ratio of ρ_{yx} between $H \parallel$ [100] and $H \parallel$ [111] at 2 K exceeds 2 in the intermediate-field region and gradually decreases as the field increases. Figure 2(f) shows the magnetization curves for $H \parallel$ [100] and $H \parallel$ [111]. At 100 K, the magnetization shows H-linear dependence and no anisotropy is observed as in ρ_{yx}. With lowering temperature, the magnetization for $H \parallel$ [100] becomes larger than that for $H \parallel$ [111]. Such an anisotropy can be attributed to the different magnetic arrangement of Tb moments.

In canonical spin-ice systems such as $Ho_2Ti_2O_7$ and its nonmagnetic-ion-doped analogs, the sufficiently large, but not too large, magnetic field along [100] ([111]) favors the 2-in 2-out (3-in 1-out) state [see Fig. 1(b)] [25,26]. Because of the single-ion anisotropy of Tb $4f$ moments along the
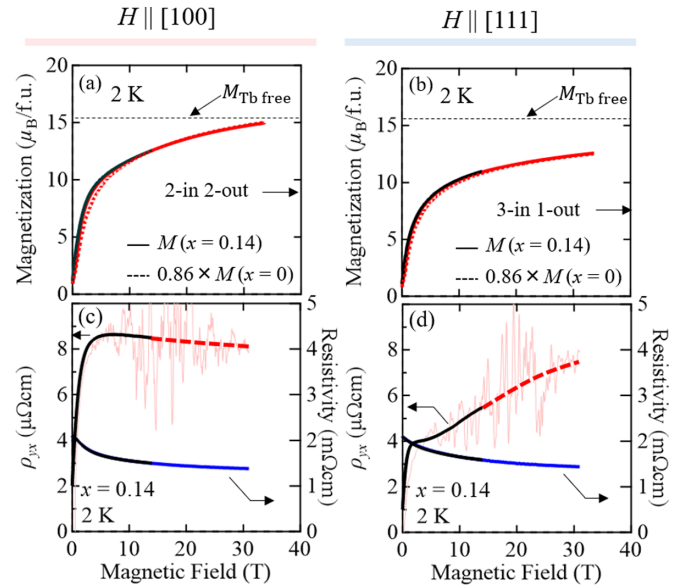

FIG. 3. Magnetic field dependence of magnetization up to 34 T for (a) $H \parallel$ [100] and (b) $H \parallel$ [111]. Magnetic field dependence of Hall resistivity as well as resistivity for (c) $H \parallel$ [100] and (d) $H \parallel$ [111]. The black curves indicate the results of dc field measurements up to 14 T. The red and blue curves show the results of high field measurements using pulsed fields up to 31 T.

local ⟨111⟩ orientation, a similar magnetic arrangement can be realized in each field direction. In fact, the expected net moment of the 2-in 2-out state is larger than that of the 3-in 1-out state by ~1.2 μ_B/f.u., which is consistent with the magnetization observed in Fig. 2(f). Such a small difference of the net magnetization between $H \parallel$ [100] and $H \parallel$ [111] cannot explain the strong anisotropy in Hall resistivity. Instead, the non-coplaner magnetic arrangement, or equivalently the scalar spin chirality, is likely to play a key role in the observed Hall effect.

In order to elucidate the origin of the Hall effect, we employ the higher magnetic field measurement which allows us to fully control the Tb moment configurations. Figure 3(a) [Fig. 3(b)] shows the magnetic field dependence of magnetization up to above 34 T at 2 K for $H \parallel$ [100] ([111]). The magnetization measured by the pulse magnet (red solid curve) perfectly overlaps with the one measured by the dc magnet (black curve). Remarkably, the magnetization for $H \parallel$ [100] monotonically increases, exceeds the expected value for the 2-in 2-out state (8.9 μ_B/f.u.) at 4 T, and nearly reaches 15.5 μ_B/f.u. at 34 T, which is expected for fully polarized Tb $4f$ moments, likely stemming from the competition between the magnetic anisotropy and the Zeeman effect. Thus, we can examine the magnetotransport properties for both collinear and noncollinear magnetic states on one sample. We also plot the magnetization for $x = 0$ in Figs. 3(a) and 3(b). To compare with that for $x = 0.14$, we normalize it by the density of Tb moments; namely, we multiply it by $1 - x = 0.86$. Notably, the normalized curve for $x = 0$ falls onto the same curve for $x = 0.14$ above 10 T, indicating that the Mo contribution to the whole magnetization is almost negligible not only for the spin-glass insulating $x = 0$ crystal but also for
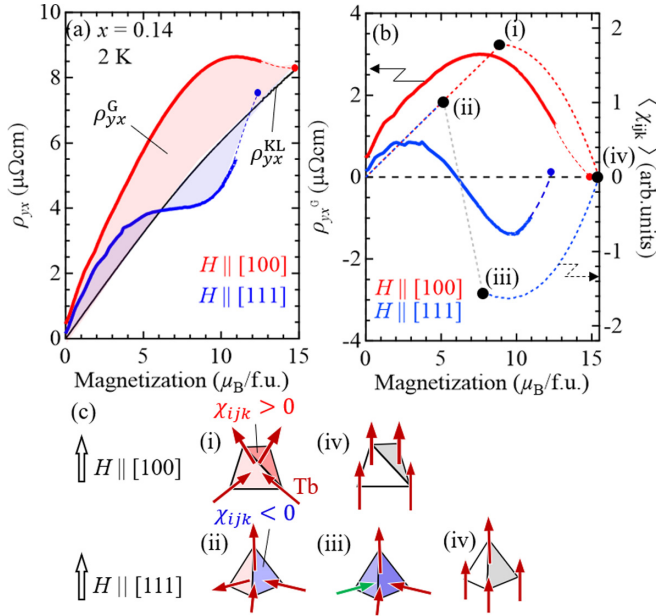
FIG. 4. (a) Magnetization dependence of the Hall resistivity. The solid lines denote the data obtained with the dc field, and the circles are the values at the maximum pulse field. The dotted lines are the smoothed data taken by the pulse field measurement. (b) Magnetization dependence of the GHE and the simulated spin chirality. Red and blue dashed lines represent the simulated SSC of the single Tb tetrahedron based on the magnetization curves (see the Appendix, Sec. 3). (c) Possible magnetic structure and SSC at each point in panel (b).

the carrier-doped metallic $x = 0.14$ one, in stark contrast to the Mo-spin ferromagnetic $Nd_2Mo_2O_7$ [4]. Figures 3(c) and 3(d) show the magnetic field dependence of resistivity and Hall resistivity for $H \parallel [100]$ and $H \parallel [111]$, respectively. The resistivity gradually decreases as the field increases up to 31 T for both field directions, as observed in the measurement in the dc magnet. The Hall resistivity data measured by the pulse magnet seem somewhat noisy, because of the small Hall signals compared to the longitudinal resistivity. Nevertheless, the overall field dependence and amplitude are reconciled with the dc data, and moreover the signal appears reliable again near the maximum field, since the data can be integrated during the relatively long time at high fields in the field pulse shape. As the field approaches 31 T, ρ_{yx} for $H \parallel [100]$ gradually decreases down to ~ 8 $\mu\Omega$ cm, while that for $H \parallel [111]$ explicitly increases up to ~ 7.5 $\mu\Omega$ cm. Apparently, the anisotropy of ρ_{yx} disappears at high magnetic fields.

In general, the Hall resistivity is expressed as

$$\rho_{yx} = R_0 \mu_0 H + R_S \rho_{xx}^n M_z + \rho_{yx}^G, \quad (1)$$

where R_0 is the ordinary Hall coefficient, $R_S \rho_{xx}^n$ is the anomalous Hall coefficient with the scaling factor n in the case of diffusive metal [27], and ρ_{yx}^G is the geometrical contribution. According to the previous study on Cd-doped $Y_2Mo_2O_7$, the ordinary Hall effect is quite small (less than 0.3 $\mu\Omega$ cm at 14 T) [28]. Therefore, we neglect here the ordinary contribution for simplicity. To extract the geometrical contribution, we plot ρ_{yx} as a function of magnetization in Fig. 4(a). The red and blue solid lines denote experimental data measured in

the dc magnetic field, red and blue circles are the data at the highest field 31 T, and red and blue dashed lines indicate the noise-smoothed connections between these two experimental data. Since the magnetization for $H \parallel [100]$ is almost saturated at 31 T [Fig. 3(a)], we can assume that the geometrical contribution is zero at 31 T. The black line in Fig. 4(a) indicates the Karplus-Luttinger-type anomalous Hall resistivity, $\rho_{yx}^{KL} = R_S \rho_{xx}^n M_z$, where $n = 0.4$ in the carrier hopping regime, as confirmed in the Appendix, Fig. 7 [27]. As can be seen, ρ_{yx} for $H \parallel [100]$ is larger than ρ_{yx}^{KL} in the whole magnetization regime. Remarkably, for $H \parallel [111]$, ρ_{yx} shows nonmonotonic magnetization dependence as opposed to ρ_{yx}^{KL}. Especially, ρ_{yx} crosses ρ_{yx}^{KL} at $M \sim 6$ μ_B/f.u. and eventually merges to ρ_{yx}^{KL} at the largest magnetization.

Figure 4(b) displays the extracted geometrical contribution, $\rho_{yx}^G = \rho_{yx} - \rho_{yx}^{KL}$, as a function of magnetization. As the magnetization increases, ρ_{yx}^G for $H \parallel [100]$ gradually increases, reaches the maximum at ~ 8 μ_B/f.u., and eventually decreases towards zero at the full moment of 15.5 μ_B/f.u. This envelope-shaped magnetization dependence of ρ_{yx}^G, which is also observed in several materials [3,29], may reflect the modulation of Tb magnetic states. Both Tb and Mo magnetic moments are disordered at zero magnetic field. As the field increases, the large Tb moments are getting aligned due to the gain of Zeeman energy under the influence of the [111] Ising anisotropy, and they eventually form a 2-in 2-out like configuration at $M \sim 8.9$ μ_B/f.u. [see panel (i) in Fig. 4(c)]. With further increasing field, the Zeeman energy gradually overcomes the magnetic anisotropy energy, and finally the Tb moments are fully aligned collinearly, as shown in panel (iv) in Fig. 4(c). Here we simulate the average of SSC $\langle \chi_{ijk} \rangle$ in a single tetrahedron having four triangle planes, as shown in Fig. 1(b) (see the Appendix, Sec. 3, for more detail). Assuming that all Tb moments simply approach are aligning to the field direction with increasing field, we can calculate the angle between Tb moments and the external field from the magnetization value and hence obtain $\langle \chi_{ijk} \rangle$. Starting from the perfect 2-in 2-out state [panel (i) in Fig. 4(c)], $\langle \chi_{ijk} \rangle$ monotonically decreases towards zero [panel (iv)in Fig. 4(c)] as the magnetization is increased. This is intuitively understandable since the solid angle subtended by Tb moments becomes smaller as the applied field is increased.

On the other hand, ρ_{yx}^G for $H \parallel [111]$ shows unique magnetization dependence. It is somewhat similar to that for $H \parallel [100]$ below 2 μ_B/f.u., but ρ_{yx}^G decreases towards the negative value as the magnetization is further increased. It takes the minimum value (negative maximum) at ~ 9 μ_B/f.u. and then approaches zero at the large magnetization value. To understand this behavior, we consider the magnetic arrangement and $\langle \chi_{ijk} \rangle$. According to the neutron diffraction experiments [30], Tb-Tb interaction in $Tb_2Mo_2O_7$ is ferromagnetic and hence favors the 2-in 2-out magnetic structure at weak magnetic fields, similar to canonical spin-ice systems $Dy_2Ti_2O_7$ and $Ho_2Ti_2O_7$ [14,31], and spin-ice-like ordered semimetal $Pr_2Ir_2O_7$ [32,33]. At the intermediate field applied along [111], the apical spins, whose easy axes are along the field direction, are fixed while the other three spins obey the ice rule, forming the so-called kagomé ice state [see panel (ii) in Fig. 4(c)]. Moreover, R moments with the strong Ising char-
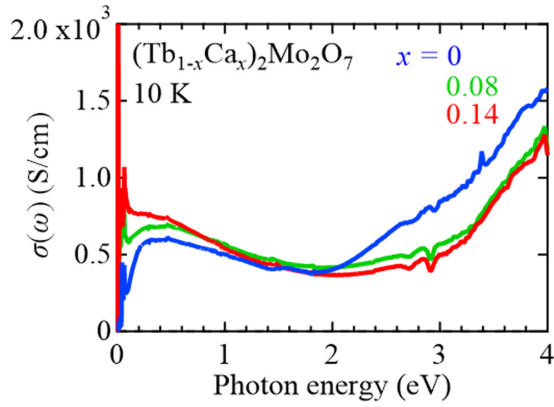
FIG. 5. Expanded energy dependence of optical conductivity spectra up to 2 eV for three compounds ($x = 0$, 0.08, and 0.14).

acter undergo the liquid-gas-type magnetic transition from the kagomé ice state to the 3-in 1-out state [panel (iii) in Fig. 4(c)] at higher fields. We speculate that the crossover between these magnetic states occurs in the present system as well, leading to the remarkable sign change of $\langle \chi_{ijk} \rangle$ and hence of ρ_{yx}^G, as shown in Fig. 4(b). In fact, the sign of $\langle \chi_{ijk} \rangle$ changes at $M \sim 6 \, \mu_B$/f.u., consistent with the experimental observation of the sign change of the GHE. While the magnetization value exceeds that for the 3-in 1-out state, we anticipate that the 3-in Tb moments in the 3-in 1-out state are forcedly aligned toward the collinear state. $\langle \chi_{ijk} \rangle$ slightly decreases and forms a broad dip centered at $\sim 10 \, \mu_B$/f.u., and then quickly increases towards zero at 15.5 μ_B/f.u.. Despite such a simplified simulation of $\langle \chi_{ijk} \rangle$, the overall magnetization dependence of ρ_{yx} can be well explained. The present experimental data clearly indicate that the GHE is controlled by the exchange fields from the configuration of the local Tb moments in the weak-coupling regime.

In conclusion, we observe the geometrical Hall effects in the pyrochlore-type $(Tb_{1-x}Ca_x)_2Mo_2O_7$ single crystal, whose conduction electrons are interacting with local magnetic moments in the weak-coupling region and thus represent the ideal platform to study the correlation between electronic transport and noncollinear magnetism. The highly field-anisotropic geometrical Hall effect can be well explained by the real-space SSC arising from the non-coplanar Tb magnetic arrangement. We clearly demonstrate that there is one-to-one correspondence between the geometrical Hall effect and the SSC, both of which vary for the occurring local magnetic states, e.g., 2-in 2-out, 3-in 1-out, and fully aligned collinear states.

APPENDIX

1. Optical conductivity spectra

Figure 5 shows the optical conductivity spectra up to 4 eV for three compounds ($x = 0$, 0.08, and 0.14). All com-
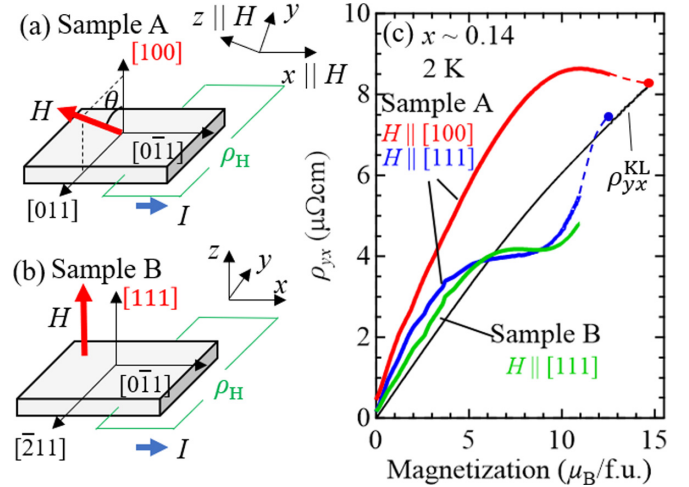

FIG. 6. Measurement setups for (a) sample A, which is mainly used for the anisotropic measurement, and (b) sample B for comparison. Each out-of-plane axis is along the [100] and [111] crystalline orientations, respectively. (c) Magnetization dependence of Hall resistivity for sample A (a) and sample B (b) setups. The red and blue curves are for sample A, and the green curve is for sample B. The black curve is the Karplus-Luttinger term of Hall resistivity. For more detail, see the main text.

pounds show the humplike structure centered at 0.4 eV which corresponds to the residue of the Mott-gap transition of the Mo $4d$ electrons [21]. The large increase of optical conductivity above 3 eV can be attributed to the charge transfer excitation.

2. Hall resistivity measurement

The magnetic anisotropy of the Hall effect was investigated by rotating sample A against the applied magnetic field, so that we could rule out the possibility of sample dependence. Figure 6(a) shows the geometry of sample A. It was polished into the platelike shape whose vertical direction is along the [100] crystalline axis. The electric current flowed along the [0$\bar{1}$1] axis, about which the magnetic field was rotated. The transverse resistivity ρ_H was measured along the [011] axis, which is perpendicular to both the [100] axis and the [0$\bar{1}$1] axis.

Let us take the magnetic field direction as the z axis and the current direction as the x axis, as depicted in Fig. 6(a). When the field is tilted by θ off the [100] direction, the Hall resistivity ρ_H is expressed as

$$\rho_H(\theta) = \rho_{yx}(\theta)\cos\theta - \rho_{zx}(\theta)\sin\theta. \quad (A1)$$

The first term is the usual Hall effect perpendicular to both the magnetic field and the current, which should be extracted from the measured value ρ_H. Considering the symmetry of the setup of Fig. 6(a), we obtain $\rho_{yx}(\theta) = \rho_{yx}(-\theta)$ and $\rho_{zx}(\theta) = \rho_{zx}(-\theta)$, while $\sin\theta$ is odd. Therefore, we can extract $\rho_{yx}(\theta)$ by averaging $\rho_H(+\theta)$ and $\rho_H(-\theta)$ and then dividing by $\cos\theta$. Figure 6(c) displays the magnetization dependence of ρ_{yx} for both [100] and [111] field directions, in which one can clearly see the anisotropy, as discussed in the main text.
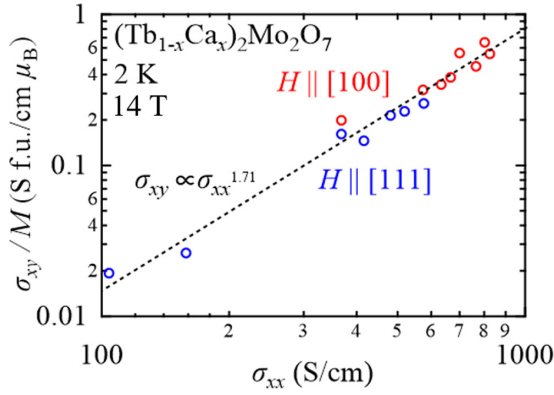
FIG. 7. Scaling plot of σ_{xy} versus σ_{xx} in the logarithmic scale. The red (blue) marks denote the data for $H\|[100]$ ($H\|[111]$). The dashed line indicates the scaling relation $\sigma_{xy} \propto \sigma{xx}^{1.71}$.

To double-check ρ_{yx} for $H\|[111]$, we prepare another sample B, whose out-of-plane axis is along the [111] crystalline direction while the current direction is the same as that in sample A ([0$\bar{1}$1]). In this geometry, we can obtain $\rho_{yx} = \rho_H$ for $H\|[111]$ without any calculation, as plotted in Fig. 6(c). Although the chemical composition of sample B ($x = 0.134$) is slightly different from that of sample A ($x = 0.140$), ρ_{yx} of sample B is remarkably similar to that of sample A for $H\|[111]$. Thus, the anisotropy discussed in the main text is ubiquitous for the present system.

3. Scaling law for Hall conductivity

In the hopping region, the anomalous Hall conductivity σ_{xy} is known to follow the empirical scaling relation $\sigma_{xy} \propto \sigma_{xx}^{1.6}$, where σ_{xx} is the longitudinal conductivity [27]. Note that ρ_{yx} is proportional to $\rho_{xx}^{0.4}$ when the Hall conductivity is much smaller than longitudinal conductivity, since $\rho_{yx} = \sigma_{xy}/(\sigma_{xx}^2 + \sigma_{xy}^2)$. Figure 7 shows σ_{xy} normalized by magnetization as a function of σ_{xx} for several different samples at 2 K and 14 T, at which the anomalous Hall contribution is dominant. One can see $\sigma_{xy} \propto \sigma_{xx}^{1.71}$ in a wide range of σ_{xx} from 10^2 to 10^3 S/cm. Therefore, we use $n = 0.4$ in Eq. (1) in the main text to estimate the Karplus-Luttinger term ρ_{yx}^{KL}.

4. Calculation of the scalar spin chirality

Since the Mo magnetization in $(Tb_{1-x}Ca_x)_2Mo_2O_7$ is negligible, as demonstrated in Fig. 2 of the main text, we can assume the magnetic structure of the Tb tetrahedra from the magnetization and hence calculate the scalar spin chirality χ_{ijk}.

First we consider the case for $H\|[100]$. At zero magnetic field, Tb magnetic moments are disordered but host 2-in 2-out (2I2O) like habit because of the ferromagnetic interaction between nearest-neighbor Tb moments. As the magnetic field increases, the number of 2I2O Tb tetrahedra, whose net magnetizations are parallel to the field direction, increases and hence the magnetization reaches the expected value of $M_{2I2O} = 2(1 - x) \times (\frac{4\mu_{Tb}}{\sqrt{3}})/4 = 10.4(1 - x)$ (μ_B/f.u.), where $\mu_{Tb} = 9$ (μ_B/Tb) [state (i) in Fig. 4(c) of the main text]. With increasing field above 2 T, we speculate that the Zeeman
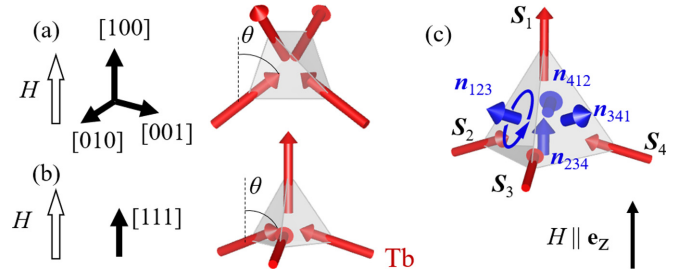

FIG. 8. Tb moment modulation for (a) $H\|[100]$ at $M \geqslant M_{2I2O}$ and (b) $H\|[111]$ at $M \geqslant M_{3I1O}$. (c) Schematic picture of the tetrahedron for the calculation of the scalar spin chirality. Red arrows indicate the spins at each site (S_1, S_2, S_3, and S_4), and blue arrows indicate the unit vectors parallel to the emergent field ($n_{123}, n_{234}, n_{341}$, and n_{412}).

energy overcomes the single-ion anisotropy and hence the Tb moments gradually approach the field direction. We define θ as the angle between the Tb moments and the magnetic field direction [Fig. 8(a)], so that the magnetization is given as $M_{100} = 2(1 - x)\mu_{Tb} \cos\theta$. In this way, we estimate the tilt angle of the Tb moment from the measured magnetization to calculate χ_{ijk} as discussed later.

The magnetization process for $H\|[111]$ is more complex. Similar to spin-ice materials, the magnetization for the [111] field direction increases with increasing field towards $M_{KI} = 2(1 - x) \times (\mu_{Tb} + \frac{\mu_{Tb}}{3})/4 = 6(1 - x)$ (μ_B/f.u.), at which the kagomé ice state is realized [state (ii) in Fig. 4(c) in the main text]. In other words, the 2-in 2-out state is preserved up to M_{KI}, resulting in nearly the same curve as the case for $H\|[100]$. Above M_{KI}, the crossover occurs from (ii) 2-in 2-out state to (iii) 3-in 1-out state, at which the magnetization becomes $M_{3I1O} = 2(1 - x) \times (\mu_{Tb} + \frac{\mu_{Tb}}{3} \times 3)/4 = 9(1 - x)$ (μ_B/f.u.). Eventually, as the field increases further, Tb moments deviate from the local $\langle 111 \rangle$ axes and get aligned collinearly [state (iv) in Fig. 4(c) of the main text]. Between (iii) and (iv) states, the magnetization is written as $M_{111} = 2(1 - x) \times (\mu_{Tb} + 3\mu_{Tb} \cos\theta)/4$, where θ is the angle between Tb moments and the field, as shown in Fig. 8(b).

Making use of the information of configurations of Tb magnetic moments as extracted above, we calculate the spin chirality of the Tb tetrahedron averaged over four Tb sites on the vertices of one tetrahedron. According to the theoretical calculation in the weak-coupling region [18], the emergent magnetic field H_{eff} acting on the Mo-conducting electrons is given as

$$H_{eff} \propto \langle \chi_{ijk} \rangle$$
$$= \frac{1}{6N} \sum_{i,j,k \in \text{all sites}} S_i \cdot (S_j \times S_k) F(r_i, r_j, r_k) \cdot e_z, \quad (A2)$$

where

$$F(r_i, r_j, r_k) = (a \times b/ab)I'(a)I'(b)I(c)$$
$$+ (b \times c/bc)I(a)I'(b)I'(c)$$
$$+ (c \times a/ca)I'(a)I(b)I'(c); \quad (A3)$$

e_z is the unit vector parallel to the field direction; r_i, r_j, and r_k are the positions of local spins at site i, j, and k; $a = r_i - r_j$,

$b = r_j - r_k$, and $c = r_k - r_i$ are the distances between each site; $I(r)$ is the rapidly decreasing function of r; and $I' = \frac{dI(r)}{dr}$. Thus we take into account only the nearest-neighbor sites 1, 2, 3, and 4 in a single tetrahedron shown in Fig. 8(c):

$$\langle \chi_{ijk} \rangle \propto \sum_{i,j,k \in 1,2,3,4} S_i \cdot (S_j \times S_k) n_{ijk} \cdot e_z, \qquad (A4)$$

where n_{ijk} is the unit vector defined by the right-hand screw rule when orbiting the sites i, j, and k. The calculated results are plotted in Fig. 4(c) in the main text. We note that the spin chirality is not calculated but just a connecting straight line drawn between M_{KI} and M_{3IIO} in $H \parallel [111]$ [states (ii) and (iii) in Figs. 4(b) and 4(c)], because the detailed magnetic state is not trivial. The calculated curves of the SSC based on the above simple assumption reasonably reproduce the experimental results of geometrical Hall components.

[1] Y. Tokura, S. Seki, and N. Nagaosa, Rep. Prog. Phys. **77**, 076501 (2014).

[2] N. Nagaosa and Y. Tokura, Nat. Nanotechnol. **8**, 899 (2013).

[3] J. Ye, Y. B. Kim, A. J. Millis, B. I. Shraiman, P. Majumdar, and Z. Tešanović, Phys. Rev. Lett. **83**, 3737 (1999).

[4] Y. Taguchi, Y. Oohara, H. Yoshizawa, N. Nagaosa, and Y. Tokura, Science **291**, 2573 (2001).

[5] N. Nagaosa, J. Sinova, S. Onoda, A. H. MacDonald, and N. P. Ong, Rev. Mod. Phys. **82**, 1539 (2010).

[6] K. Ohgushi, S. Murakami, and N. Nagaosa, Phys. Rev. B **62**, R6065(R) (2000).

[7] Z. Fang, N. Nagaosa, K. S. Takahashi, A. Asamitsu, R. Mathieu, T. Ogasawara, H. Yamada, M. Kawasaki, Y. Tokura, and K. Terakura, Science **302**, 92 (2003).

[8] A. Neubauer, C. Pfleiderer, B. Binz, A. Rosch, R. Ritz, P. G. Niklowitz, and P. Böni, Phys. Rev. Lett. **102**, 186602 (2009).

[9] N. Kanazawa, Y. Onose, T. Arima, D. Okuyama, K. Ohoyama, S. Wakimoto, K. Kakurai, S. Ishiwata, and Y. Tokura, Phys. Rev. Lett. **106**, 156603 (2011).

[10] T. Katsufuji, H. Y. Hwang, and S.-W. Cheong, Phys. Rev. Lett. **84**, 1998 (2000).

[11] S. Iguchi, N. Hanasaki, M. Kinuhara, N. Takeshita, C. Terakura, Y. Taguchi, H. Takagi, and Y. Tokura, Phys. Rev. Lett. **102**, 136407 (2009).

[12] J. S. Gardner, M. J. P. Gingras, and J. E. Greedan, Rev. Mod. Phys. **82**, 53 (2010).

[13] N. Ali, M. P. Hill, S. Labroo, and J. E. Greedan, J. Solid State Chem. **83**, 178 (1989).

[14] M. J. Harris, S. T. Bramwell, D. F. McMorrow, T. Zeiske, and K. W. Godfrey, Phys. Rev. Lett. **79**, 2554 (1997).

[15] S. T. Bramwell and M. J. P. Gingras, Science **294**, 1495 (2001).

[16] Y. Taguchi, T. Sasaki, S. Awaji, Y. Iwasa, T. Tayama, T. Sakakibara, S. Iguchi, T. Ito, and Y. Tokura, Phys. Rev. Lett. **90**, 257202 (2003).

[17] M. Hirschberger, Y. Nomura, H. Mitamura, A. Miyake, T. Koretsune, Y. Kaneko, L. Spitz, Y. Taguchi, A. Matsuo, K. Kindo, R. Arita, M. Tokunaga, and Y. Tokura, Phys. Rev. B **103**, L041111 (2021).

[18] G. Tatara and H. Kawamura, J. Phys. Soc. Jpn. **71**, 2613 (2002).

[19] K. Ueda, S. Iguchi, T. Suzuki, S. Ishiwata, Y. Taguchi, and Y. Tokura, Phys. Rev. Lett. **108**, 156601 (2012).

[20] Y. Kaneko and Y. Tokura, J. Cryst. Growth **533**, 125435 (2020).

[21] I. Kézsmárki, N. Hanasaki, K. Watanabe, S. Iguchi, Y. Taguchi, S. Miyasaka, and Y. Tokura, Phys. Rev. B **73**, 125122 (2006).

[22] M. T. Vandenborre, E. Husson, J. P. Chatry, and D. Michel, J. Raman Spectrosc. **14**, 63 (1983).

[23] K. Taniguchi, T. Katsufuji, S. Iguchi, Y. Taguchi, H. Takagi, and Y. Tokura, Phys. Rev. B **70**, 100401(R) (2004).

[24] K. Ueda, R. Kaneko, A. Subedi, M. Minola, B. J. Kim, J. Fujioka, Y. Tokura, and B. Keimer, Phys. Rev. B **100**, 115157 (2019).

[25] H. Liu, J. Bian, S. Chen, Y. Feng, Y. Xie, and B. Fang, J. Magn. Magn. Mater. **465**, 316 (2018).

[26] G. Ehlers, J. S. Gardner, C. H. Booth, M. Daniel, K. C. Kam, A. K. Cheetham, D. Antonio, H. E. Brooks, A. L. Cornelius, S. T. Bramwell, J. Lago, W. Häussler, and N. Rosov, Phys. Rev. B **73**, 174429 (2006).

[27] T. Miyasato, N. Abe, T. Fujii, A. Asamitsu, S. Onoda, Y. Onose, N. Nagaosa, and Y. Tokura, Phys. Rev. Lett. **99**, 086602 (2007).

[28] S. Iguchi, Y. Kumano, K. Ueda, S. Kumakura, and Y. Tokura, Phys. Rev. B **84**, 174416 (2011).

[29] K. K. Kolincio, M. Hirschberger, J. Masell, S. Gao, A. Kikkawa, Y. Taguchi, T.-h. Arima, N. Nagaosa, and Y. Tokura, Proc. Natl. Acad. Sci. USA **118**, e2023588118 (2021).

[30] G. Ehlers, J. E. Greedan, J. R. Stewart, K. C. Rule, P. Fouquet, A. L. Cornelius, C. Adriano, P. G. Pagliuso, Y. Qiu, and J. S. Gardner, Phys. Rev. B **81**, 224405 (2010).

[31] T. Sakakibara, T. Tayama, Z. Hiroi, K. Matsuhira, and S. Takagi, Phys. Rev. Lett. **90**, 207205 (2003).

[32] D. E. MacLaughlin, O. O. Bernal, L. Shu, J. Ishikawa, Y. Matsumoto, J.-J. Wen, M. Mourigal, C. Stock, G. Ehlers, C. L. Broholm, Y. Machida, K. Kimura, S. Nakatsuji, Y. Shimura, and T. Sakakibara, Phys. Rev. B **92**, 054432 (2015).

[33] K. Ueda, H. Ishizuka, M. Kriener, S. Kitou, D. Maryenko, M. Kawamura, T.-h. Arima, M. Kawasaki, and Y. Tokura, Phys. Rev. B **105**, L161102 (2022).